Supplementary Information : A hyperelastic oscillatory Couette system

Tejaswin Parthasarathy[1], Yashraj Bhosale[1], and Mattia Gazzola[1]†

[1]Mechanical Sciences and Engineering, University of Illinois at Urbana-Champaign, Urbana, IL 61801, USA

(Received xx; revised xx; accepted xx)

1. Details of linear Kelvin–Voigt analytical solution

Here we detail the analytical solution in case of a linear Kelvin–Voigt solid. The solution is

$$\hat{v}_f(\tilde{y}) = A\exp\left(k_f\frac{\tilde{y}}{L_f}\right) + B\exp\left(-k_f\frac{\tilde{y}}{L_f}\right) \qquad \tilde{y}\in[0,L_f)$$
$$\hat{u}_s(y) = C\exp\left(k_s\frac{y}{L_s}\right) + D\exp\left(-k_s\frac{y}{L_s}\right) \qquad y\in[0,L_s),$$

where we determine the coefficients A, B, C, D using the boundary (Main text Eq. 2.8) and interface conditions (Main text Eq. 2.7), which lead to the following system of equations

$$\begin{pmatrix} e^{k_f} & e^{-k_f} & 0 & 0 \\ 1 & 1 & -i\omega e^{k_s} & -i\omega e^{-k_s} \\ 1 & -1 & M_{33} & M_{34} \\ 0 & 0 & 1 & 1 \end{pmatrix} \cdot \begin{pmatrix} A \\ B \\ C \\ D \end{pmatrix} = \begin{pmatrix} \hat{V}_{\text{wall}} \\ 0 \\ 0 \\ 0 \end{pmatrix}, \tag{1.1}$$

with

$$M_{33} = -i\omega\frac{k_s}{k_f}\frac{L_f}{L_s}\left[\left(\frac{\nu_s}{\nu_f}\right)\left(\frac{\rho_s}{\rho_f}\right) - i\left(\frac{2c_1}{\omega\mu_f}\right)\right]\exp(k_s)$$
$$M_{34} = +i\omega\frac{k_s}{k_f}\frac{L_f}{L_s}\left[\left(\frac{\nu_s}{\nu_f}\right)\left(\frac{\rho_s}{\rho_f}\right) - i\left(\frac{2c_1}{\omega\mu_f}\right)\right]\exp(-k_s) \tag{1.2}$$

† Email address for correspondence: mgazzola@illinois.edu

which we can solve for to yield the final solutions. The resulting coefficients are

$$
\begin{aligned}
k_f &= \frac{(1+i)}{\sqrt{2}}\left(L_f^{-1}\left(\nu_f/\omega\right)^{0.5}\right)^{-1} = \exp\left(i\pi/4\right)\delta_f^{-1} \\
k_s &= \frac{i}{\sqrt{\left(\left(\omega L_s\right)^{-1}\left(2c_1/\rho_s\right)^{0.5}\right)^2 + i\left(L_s^{-1}\left(\nu_s/\omega\right)^{0.5}\right)^2}} = i\left(\lambda^2 + i\delta_s^2\right)^{-0.5} \\
\alpha &= \frac{L_f}{L_s}\frac{k_s}{k_f}\left(\rho\nu - i\frac{\dot{\gamma}}{Er}\right) \\
A &= \hat{V}_{\text{wall}}\frac{\left[\left(e^{-k_s}\right)(1-\alpha) - \left(e^{+k_s}\right)(1+\alpha)\right]}{\left[\left(e^{k_f-k_s} - e^{-(k_f-k_s)}\right)(1-\alpha) - \left(e^{k_f+k_s} - e^{-(k_f+k_s)}\right)(1+\alpha)\right]} \\
B &= \hat{V}_{\text{wall}}\frac{\left[\left(-e^{k_s}\right)(1-\alpha) + \left(e^{-k_s}\right)(1+\alpha)\right]}{\left[\left(e^{k_f-k_s} - e^{-(k_f-k_s)}\right)(1-\alpha) - \left(e^{k_f+k_s} - e^{-(k_f+k_s)}\right)(1+\alpha)\right]} \\
C &= \frac{-2\hat{V}_{\text{wall}}}{i\omega}\frac{1}{\left[\left(e^{k_f-k_s} - e^{-(k_f-k_s)}\right)(1-\alpha) - \left(e^{k_f+k_s} - e^{-(k_f+k_s)}\right)(1+\alpha)\right]} \\
D &= -C
\end{aligned}
\tag{1.3}
$$

We note here that k_f and k_s denote the fluid and solid wave contributions and α represents the degree of fluid–solid coupling.

2. Piecewise linear functions as particular solutions

Here, we motivate the natural choice of using piecewise linear functions in our series solution for the fluid and solid domains (Main text Eq. 3.5), in addition to the Fourier sine series. Indeed, if we consider the simpler Couette flow case, i.e. only viscous fluid between two parallel plates (at $L = 0$ and $L = L_{\text{wall}}$, with the top wall moving with V_{wall}), the *trivial* solution lying in the nullspace of the governing continuity and momentum equations (Main text Eq. 2.4) is $v(y) = V_{\text{wall}}y/L_{\text{wall}}$. Formally, this trivial solution is a particular solution of the governing linear PDE, arising due to an inhomogeneity caused by a non-zero wall velocity (boundary conditions and forcing terms are interchanged by Duhamel's principle). One can then view Eq. 3.5 as a superposition of the particular solution and homogeneous solution to the governing PDE.

3. Useful identities in Fourier bases

We proceed by utilizing the following orthogonality and integral relations for Fourier basis functions, given $k, l \neq 0$

$$
\begin{aligned}
&\text{Orthogonality relations} && \int_0^L \sin\frac{\pi k y}{L}\sin\frac{\pi l y}{L}dy = \frac{L}{2}\delta_{kl} \\
& && \int_0^L \cos\frac{\pi k y}{L}\cos\frac{\pi l y}{L}dy = \frac{L}{2}\delta_{kl} \\
&\text{Integral relations} && \int_0^L \sin\frac{\pi k y}{L} = \frac{L}{\pi k}\left[1-(-1)^k\right] \\
& && \int_0^L \frac{y}{L}\sin\frac{\pi k y}{L} = \frac{L}{\pi k}\left(-(-1)^k\right)
\end{aligned}
\tag{3.1}
$$

where δ_{kl} is the delta function, used in a pointwise sense.

4. Details of linear Kelvin–Voigt modal solution

Here we detail the closed-form modal solution in the case of a linear Kelvin–Voigt solid. We represent the solution $u(y,t), v(y,t)$ using the Fourier sine series only in the upper half space $y \geq 0$, as follows

$$\begin{aligned} v_f(\tilde{y},t) &= V_I(t) + \frac{\tilde{y}}{L_f}\left(V_{\text{wall}}(t) - V_I(t)\right) + \sum_{k=1}^{\infty} v_{f,k}(t)\sin\frac{\pi k\tilde{y}}{L_f} \\ u_s(y,t) &= \frac{U_I(t)y}{L_s} + \sum_{k=1}^{\infty} u_{s,k}(t)\sin\frac{\pi k y}{L_s} \end{aligned} \tag{4.1}$$

where $U_I(t), V_I(t)$ is the displacement and velocity of the solid–fluid interface at $y = L_s$, $\tilde{y} = y - L_s$, and $v_{f,k}(t)$ and $u_{s,k}(t)$ are the Fourier expansion coefficients of v_f and u_s, respectively.

$$\begin{aligned} V_I(t) &= \text{Im}\left[\hat{V}_I \exp(i\omega t)\right] \\ v_{f,k}(t) &= \text{Im}\left[\hat{v}_{f,k}\exp(i\omega t)\right] \\ u_{s,k}(t) &= \text{Im}\left[\hat{u}_{s,k}\exp(i\omega t)\right], \end{aligned}$$

with the immediate implication that

$$\begin{aligned} U_I(t) &= \text{Im}\left[\frac{\hat{V}_I}{i\omega}\exp(i\omega t)\right] \\ v_{s,k}(t) = \frac{\mathrm{d}u_{s,k}}{\mathrm{d}t} &= \text{Im}\left[i\omega\hat{u}_{s,k}\exp(i\omega t)\right] \\ \frac{\mathrm{d}^2u_{s,k}}{\mathrm{d}t^2} &= \text{Im}\left[-\omega^2\hat{u}_{s,k}\exp(i\omega t)\right]. \end{aligned}$$

Substitution of the temporal transformed quantities above in the momentum ODEs and considering the boundary, interface conditions give the following expression for $\hat{v}_{f,k}, \hat{u}_{s,k}, \hat{V}_I$.

$$\begin{aligned} \hat{v}_{f,k} &= \frac{\left\{(-1)^k\hat{V}_{\text{wall}} - \hat{V}_I\right\}\alpha_k}{\pi k} \\ \hat{u}_{s,k} &= -\frac{i(-1)^k\hat{V}_I\beta_k}{\pi\omega k} \\ \hat{V}_I &= \frac{\hat{V}_{\text{wall}}\left(1 + \sum_{k=1}^{K-1}(-1)^k\alpha_k\right)}{\left(1 + \sum_{k=1}^{K-1}\alpha_k\right) + \left(\frac{L_f}{L_s}\right)\left[\left(\frac{\nu_s}{\nu_f}\right)\left(\frac{\rho_s}{\rho_f}\right) - i\left(\frac{2c_1}{\omega\mu_f}\right)\right]\left(1 + \sum_{k=1}^{K-1}\beta_k\right)} \end{aligned}$$

where

$$\begin{aligned} \alpha_k &= \frac{2}{1 - i\pi^2k^2\left({L_f}^{-1}\left(\nu_f/\omega\right)^{0.5}\right)^2} \\ \beta_k &= \frac{2}{1 - \pi^2k^2\left[\left((\omega L_s)^{-1}\left(2c_1/\rho_s\right)^{0.5}\right)^2 + i\left({L_s}^{-1}\left(\nu_s/\omega\right)^{0.5}\right)^2\right]}. \end{aligned}$$

The expressions above can then be directly used in Eq. 4.1 to analytically evaluate solid displacements, fluid velocities and solid velocities, respectively.

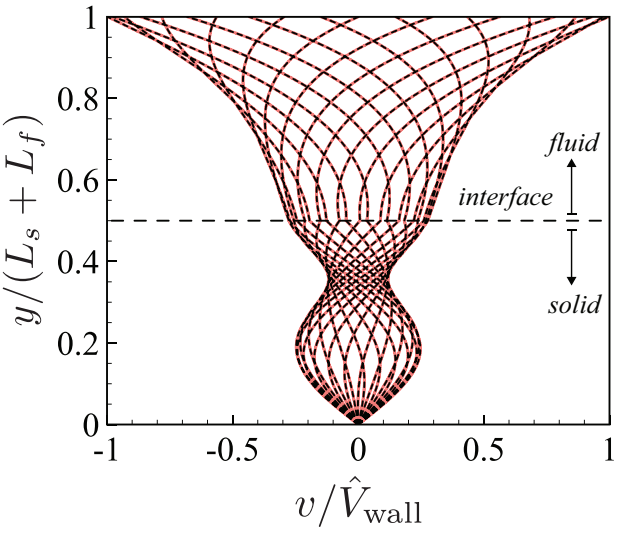

Figure 1: Comparison of direct analytical and modal solutions. Plotting the non-dimensional velocity profiles for a linear Kelvin–Voigt solid using the direct analytical (solid red line) and modal solutions (dashed black line) reveals good agreement across all times. The system is characterized by the same parameters as Figure 3 in the main text.

5. Comparison of direct analytical and modal solutions

Here, we showcase comparison between our direct analytical solutions discussed in Section 1 and modal solutions discussed in Section 4 for a representative set of parameters. We overlay the velocity profiles obtained by these methods in Fig. 1 to see favorable comparison across all time instants. Hence our solutions, although obtained via different approaches, give the same results.

6. Parameter details

Here, for the purposes of repeatability and reproducibility, we document the parameter sets used to generate the results shown in the figures of our manuscript. We list the figure first and then tabulate the parameters used.

6.1. *Figure 2*

The parameters used in this figure are $Re = 0.25$, $Er = 1/(5\pi)$, $\nu = 0$, $\delta_f = 1.12$, $\delta_s = 0$, $\lambda = 2.52$, $L = 2$, $L_s = L_f = L/4$, $\rho_f = \rho_s = 1$, $\mu_f = 1.0$, $\mu_s = 0.0$, $c_1 = 2.5$, $c_3 = 0$, $\hat{V}_{\text{wall}} = 1.0$, $\omega = \pi$, $\dot{\gamma} = \pi^{-1}$.

6.2. *Figure 3*

The system here is characterized by $Re = 2$, $Er = 1$, $\nu = 0.1$, $\delta_f = 0.4$, $\delta_s = 0.126$, $\lambda = 0.225$, $L = 0.8$, $L_s = L_f = L/4 = 0.2$, $\rho_f = \rho_s = 1$, $\mu_f = 0.02$, $\mu_s = 0.1\mu_f$, $c_1 = 0.01$, $c_3 = 0$, $\hat{V}_{\text{wall}} = 0.4$, $\omega = \pi$, $\dot{\gamma} = \pi^{-1}$.

6.3. *Figure 6*

The system here is characterized by $Re = 2, Er = 1, \nu = 0.1, c = c_3/c_1 = 4, \delta_f = 0.4, \delta_s = 0.126, \lambda = 0.225$, $L = 0.8$, $L_s = L_f = L/4 = 0.2$, $\rho_f = \rho_s = 1$, $\mu_f = 0.02$, $\mu_s = 0.1\mu_f$, $c_1 = 0.01$, $c_3 = 0.04$, $\hat{V}_{\text{wall}} = 0.4$, $\omega = \pi$, $\dot{\gamma} = \pi^{-1}$.

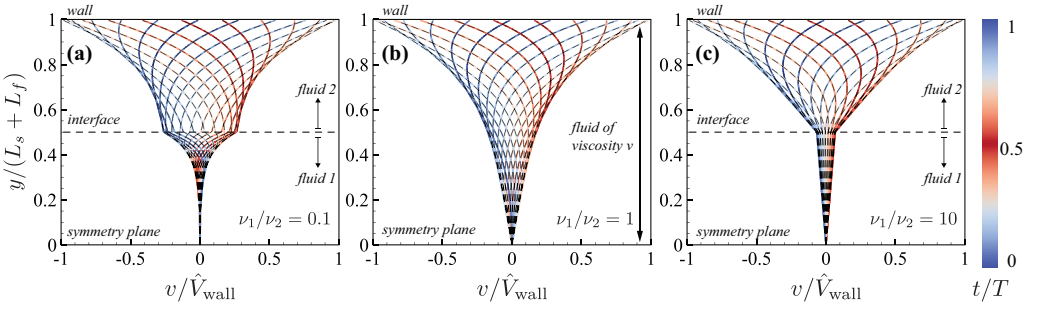

Figure 2: No elastic limit. Non-dimensional velocity profile in y when the solid is replaced by a viscous fluid. The system response is shown only for the upper half plane, for viscosity ratios $\nu = \nu_1/\nu_2 =$ (*a*) 0.1, (*b*) 1 and (*c*) 10. We compare our results with the reference Stokes–Couette solution (Landau & Lifshitz 1987) in (*b*) and two-fluid Stokes–Couette solution (Sim 2006; Leclaire *et al.* 2014) in (*a*) and (*c*). The reference solutions are shown in black dashed lines, and we find them in agreement with our solution. This system is characterized by $Re = 2, \delta = 0.4$. Other parameters used are $L_s = L_f = L/4 = 0.2$, $\rho_f = \rho_s = 1$, $\mu_f = 0.02$, $c_1 = 0$, $c_3 = 0$, $\hat{V}_{\text{wall}} = 0.4$, $\omega = \pi$. Colors represent t/T.

The parameters used for the 2D DNS are LCFL = 0.05, CFL = 0.1 with a resolution of $[512]^2$ in a domain of physical extent $[0, 1]^2$. We employ periodic and unbounded boundary conditions in the x and y directions, respectively. The periodic boundary condition allows us to impose homogeneity in the x direction. In all cases shown, the system starts from rest in a stress free state and the simulation is run well beyond the initial transient phase, resulting in periodic dynamics. The reader is referred to Bhosale *et al.* (2021) for more simulation details, and for interpretation of the CFL, LCFL and resolution parameters.

7. Details on limit cases

Here, we present comparison with available analytical solutions in the limit of $c_1 = 0$, as discussed in the main text. This limit indicates an absence of elastic forces in the solid phase. Hence, only viscous forces operate in the solid, effectively rendering it a Newtonian fluid. First, if $c_1 = 0$ and $\mu_s = \mu_f = \mu$ and $\rho_s = \rho_f = \rho$, i.e. when the entire domain is occupied by a single fluid, we recover the Stokes–Couette flow solution (Landau & Lifshitz 1987) valid throughout the domain. This is confirmed in Fig. 2b, where we see how our solution well agrees with the reference Stokes–Couette solutions, depicted in black dashed lines. Details on the reference Stokes–Couette solution can be found in Section 7.1.

Next, still within the $c_1 = 0$ limit but now with $\mu_s \neq \mu_f$ or $\rho_s \neq \rho_f$, i.e. with the domain occupied by two different fluids, we recover the multi-phase Stokes–Couette flow for two immiscible liquids, which has established piecewise (in the two fluid domains) analytical solutions (Sim 2006; Leclaire *et al.* 2014) found in Section 7.2. We showcase our solutions for two viscosity ratios $\nu = \nu_1/\nu_2 = 0.1$ and $\nu = 10$ in Fig. 2a,c, where subscripts 1, 2 indicate the bottom and top fluid respectively. Additionally, we overlay the reference solutions as black dashed lines. As can be seen, we find favorable agreement across all times.

In all cases, $Re = \dot{\gamma}\omega L_2^2/\nu_2 = 2 \sim O(1)$ and so we expect inertial and viscous contributions to be approximately equally important. Note that here the system Reynolds number is defined through the viscosity ν_2 of fluid-2. Further, $\delta_2 = 0.4$ which indicates that boundary layer effects operate in the bulk of fluid-2. This leads to moderate velocity curvatures and magnitude decay in fluid-2 across Fig. 2a,b,c. In the first case of Fig. 2a, fluid-1 is ten times less viscous than fluid-2. This leads to relatively high velocity gradients of fluid-1 at the interface

compared to fluid-2, reflecting the stress continuity condition (Main text Eq. 2.7)

$$\frac{\partial_y v_1}{\partial_y v_2} = \frac{\nu_2}{\nu_1}. \tag{7.1}$$

The low viscosity of fluid-1 additionally implies a sharper fluid-1 boundary layer at the interface with $\delta_1 = 0.13$. Consequently, the velocity profiles have significant curvature within this layer in order for viscous forces to dissipate velocities to zero at the symmetry plane. In the second case (Fig. 2b), where $\nu_1 = \nu_2$ implies a single fluid, the velocity profiles are smooth at all points in the domain and approach zero at the symmetry plane with a nearly linear profile outside the wall boundary layer ($\delta = 0.4$). Meanwhile, in the third case of Fig. 2c, fluid-1 is ten times more viscous than fluid-2. This time the gradient jump (Eq. 7.1) across the interface in fluid-1 is comparatively smaller, which results in smaller fluid-1 oscillations. The high viscosity of fluid-1 leads to a boundary layer much larger than the fluid layer thickness, with $\delta_1 = 1.26$. Hence, the velocity profiles are linear.

7.1. *Reference solution in the one fluid (no elastic solid) limit*

In the limit of $c_1 = 0$ and $\mu_s = \mu_f = \mu$ and $\rho_s = \rho_f = \rho$, i.e. when the entire domain is occupied by a fluid of kinematic viscosity ν, we recover the Stokes–Couette flow solution (Landau & Lifshitz 1987) below

$$v(y,t) = \hat{V}_{\text{wall}} \text{Im}\left[\frac{\sin(ky)}{\sin(k(L_s+L_f))}\exp(i\omega t)\right]; \quad k = \frac{1-i}{\sqrt{2}}\sqrt{\frac{\omega}{\nu}}$$

valid throughout the domain. We showcased the comparison of this solution with our results in Fig. 2b.

7.2. *Reference solution in the two fluid (no elastic solid) limit*

In the limit of $c_1 = 0$, but now with $\mu_s \neq \mu_f$ or $\rho_s \neq \rho_f$, i.e. with the domain occupied by two different fluids, we recover the multi-phase Stokes–Couette flow between two immiscible liquids, which has established piecewise (in the two fluid domains) analytical solutions (Sim 2006; Leclaire *et al.* 2014).

The solutions, for a setup with $L_1 = L_2 = L/2$, is given by

$$\begin{aligned} v_1(\hat{y},t) &= \hat{V}_{\text{wall}} \text{Im}\left[\left(C_{12}\exp\left(\lambda_1\hat{y}\right) + C_{11}\exp\left(-\lambda_1\hat{y}\right)\right)\exp(i\omega t)\right] \quad \hat{y}\in[-1,0) \\ v_2(\hat{y},t) &= \hat{V}_{\text{wall}} \text{Im}\left[\left(C_{22}\exp\left(\lambda_2\hat{y}\right) + C_{21}\exp\left(-\lambda_2\hat{y}\right)\right)\exp(i\omega t)\right] \quad \hat{y}\in[0,1], \end{aligned} \tag{7.2}$$

where $\hat{y} = 2y/L - 1$ and

$$\begin{aligned} \lambda_1 &= (1+i)\sqrt{Re_1/2} \\ \lambda_2 &= (1+i)\sqrt{Re_2/2}, \end{aligned} \tag{7.3}$$

with $Re_1 = \dfrac{\omega L^2}{4\nu_1}, Re_2 = \dfrac{\omega L^2}{4\nu_2}$. We determine the constants $C_{11}, C_{12}, C_{21}, C_{22}$ using the boundary and interface conditions, which leads to the following system of equations

$$\begin{pmatrix} e^{\lambda_2} & e^{-\lambda_2} & 0 & 0 \\ 1 & 1 & -1 & -1 \\ \lambda_2 & -\lambda_2 & M_{33} & M_{34} \\ 0 & 0 & e^{-\lambda_1} & e^{\lambda_1} \end{pmatrix} \cdot \begin{pmatrix} C_{22} \\ C_{21} \\ C_{12} \\ C_{11} \end{pmatrix} = \begin{pmatrix} 1 \\ 0 \\ 0 \\ 0 \end{pmatrix}, \tag{7.4}$$

Parameter	Minimum	Maximum
	Experimentally set quantities	
$\dot{\gamma}$	0.01 (Shankaran & Neelamegham 2001)	100 (Shankaran & Neelamegham 2001)
ω	$2\pi 0.1$ rad s^{-1} (Wu *et al.* 2018)	$2\pi 10$ rad s^{-1} (Wu *et al.* 2018)
L_f	10 µm (Desprat *et al.* 2006)	100 µm (Duncombe *et al.* 2015)
ν_f	1×10^{-6} m^2/s (Cheng 2008)	1×10^{-3} m^2/s (Cheng 2008)
ρ_f	1×10^3 kg/m^3 (Volk & Kähler 2018)	1.3×10^3 kg/m^3 (Volk & Kähler 2018)
G	1×10^3 Pa (Guimarães *et al.* 2020)	15×10^3 Pa (Guimarães *et al.* 2020)
	Derived quantities	
Re	$2\pi \cdot 10^{-12}$	$2\pi \cdot 10^{1}$
Er	$4.19 \cdot 10^{-10}$	$8.1 \cdot 10^{0}$

Table 1: Range of parameters

with

$$M_{33} = -\frac{Re_2}{Re_1}\frac{\rho_1}{\rho_2}\lambda_1$$
$$M_{34} = +\frac{Re_2}{Re_1}\frac{\rho_1}{\rho_2}\lambda_1 \tag{7.5}$$

which we then solve for. We showcased the comparison of this solution with our results in Fig. 2a,c. We remark that this setup is especially suited as a benchmark for two-fluid simulations since the interface does not deform (due to symmetry) and so curvature effects (such as those encountered while modeling surface tension effects) are identically absent. Hence only the terms contributing to interfacial stress jump are tested.

8. Range of non-dimensional parameters

Here we report our procedure for choosing the range of non-dimensional parameters in the main text. We first tabulate the potential range of parameters reported in literature for settings involving soft, biological tissues in Table 1. For angular frequencies, we assume values similar to parallel-plate cell visco-meters (Wu *et al.* 2018). We employ previously reported wall shear rates in biological soft tissue contexts (Shankaran & Neelamegham 2001). We assume that the device length scale varies between values reported for parallel plate rheometers (Desprat *et al.* 2006) and other microfluidic devices employed in cell biology (Duncombe *et al.* 2015). Next, for the fluid, we consider an aqueous glycerol solution, as it is biologically inert and cost-effective (Ayoub & Abdullah 2012). This choice is reflected in the viscosity (Cheng 2008) and density (Volk & Kähler 2018) ranges for the fluid, from pure water to pure glycerol. Finally, the elastic shear modulus values we employ is consistent with those of soft cells and tissues (Guimarães *et al.* 2020).

Then, based on the above experimentally-controlled quantities, we derive ranges for the non-dimensional parameters Re, Er, showcased in Table 1. We then choose a subset that showcases the system's dynamic richness, while spanning two orders of magnitude. This range corresponds to $Re \in [0.1, 10]$ and $Er \in [0.1, 10]$.

9. Details on the numerical solution for a nonlinear Kelvin–Voigt solid

Here, we expand on the steps in deriving the numerical solution for a nonlinear Kelvin–Voigt solid. To make the content clear and presentable, we repeat some information provided in the main text.

In the case of a nonlinear Kelvin–Voigt solid, characterized by $c_3 \neq 0$, the hyperelastic stress is proportional to the cubic power of strain in Main text Eq. 2.6 which signifies a higher order (w.r.t strain) non-linear response to deformations. In this case a numerical solution can be derived. First, we calculate the modal expansion coefficients of the nonlinear stresses $\sigma_{\mathrm{NL},k}$ in the governing equation Eq. 3.10 from the main text. For this calculation we employ a Fourier pseudospectral collocation scheme (Sugiyama *et al.* 2011). The following cosine orthogonality relation is useful in this case

$$\int_0^L \cos\frac{\pi k y}{L}\cos\frac{\pi l y}{L}dy = \frac{L}{2}\delta_{kl}\,(1+\delta_{k0}) \tag{9.1}$$

Then upon transforming Main text Eq. 3.8 into the Fourier cosine bases and using Eq. 9.1, we obtain the following expression for $\sigma_{\mathrm{NL},k}$

$$\sigma_{\mathrm{NL},k} \approx \frac{8c_3}{K\,(1+\delta_{k0})}\sum_{j=0}^{K-1}\left\{\frac{U_I}{L_s}+\sum_{l=1}^{K-1}\frac{\pi l u_{s,l}}{L_s}\cos\frac{\pi l\left(j+\frac{1}{2}\right)}{K}\right\}^3\cos\frac{\pi k\left(j+\frac{1}{2}\right)}{K} \tag{9.2}$$

which is approximate, with numerical errors incurred from truncation (discussed in Main text Section 3.2) and our choice of collocated quadrature, which is associated with the spatial discretization and sampling of the nonlinear term $(\partial u_s/\partial y)^3$ at a finite set of points $x_j = (j+\frac{1}{2})\Delta x$, with $\Delta x = L_s/K$.

Next, we employ a numerical time integration scheme to evolve the non-linear Eqs. (3.9) and (3.10) from the main text. We use a second order constant timestepper comprised of mixed Crank-Nicolson (implicit, for stability in the viscous updates) and explicit Nyström (midpoint rule) for the higher order time derivatives (Hairer *et al.* 1991). The n^{th} time level at $t = n\Delta t$ is denoted by a superscript (n). First, the prescribed wall velocity is

$$V_{\mathrm{wall}}^{(n+1)} := V_{\mathrm{wall}}((n+1)(\Delta t)) = \mathrm{Im}\left[\hat{V}_{\mathrm{wall}}\exp(i\omega\,((n+1)\Delta t))\right] \tag{9.3}$$

For the U_I update, which proceeds independently of the governing Eqs. (3.9) and (3.10) from the main text, we use the Crank-Nicolson scheme (Hairer *et al.* 1991), shown below

$$U_I^{(n+1)} \approx U_I^{(n)} + \frac{\Delta t}{2}\left(V_I^{(n+1)}+V_I^{(n)}\right)+O\left(\Delta t^2\right) \tag{9.4}$$

We then turn our attention to the modal fluid momentum equation (Main text Eq. 3.9). For updating the fluid velocity modes with the action of the viscous terms, we once again utilize the Crank-Nicolson discretization at time level n

$$\begin{aligned}&\frac{2}{\pi k}\left\{\frac{V_I^{(n+1)}-V_I^{(n)}}{\Delta t}-(-1)^k\frac{V_{\mathrm{wall}}^{(n+1)}-V_{\mathrm{wall}}^{(n)}}{\Delta t}\right\}+\frac{v_{f,k}^{(n+1)}-v_{f,k}^{(n)}}{\Delta t}\\ &=-\nu_f\left(\frac{\pi k}{L_f}\right)^2\frac{1}{2}\left(v_{f,k}^{(n+1)}+v_{f,k}^{(n)}\right)+O\left(\Delta t^2\right)\end{aligned} \tag{9.5}$$

where we note that both wall and interface velocities on the LHS are discretized consistently with $v_{f,k}$. Rearranging the terms in the equation above results in the following fluid mode

update, accurate up to second order in Δt

$$v_{f,k}^{(n+1)} = \frac{E_{f,k}}{\zeta_{f,k}} \tag{9.6}$$

where

$$E_{f,k} = \left(2 - \zeta_{f,k}\right) v_{f,k}^{(n)} - \frac{2\left\{V_I^{(n+1)} - V_I^{(n)} - (-1)^k \delta V_{\text{wall}}\right\}}{\pi k} \tag{9.7}$$

$$\zeta_{f,k} = 1 + \nu_f \frac{\Delta t}{2} \left(\frac{\pi k}{L_f}\right)^2 \tag{9.8}$$

with

$$\delta V_{\text{wall}} = V_{\text{wall}}^{(n+1)} - V_{\text{wall}}^{(n)} \tag{9.9}$$

Next, we focus on the modal solid momentum equation (Main text Eq. 3.10). Here, for updating solid displacements, we utilize the following explicit Nyström (midpoint rule) discretizations at the n^{th} time step

$$\left(\frac{\mathrm{d}V_I}{\mathrm{d}t}\right)^{(n)} \approx \frac{V_I^{(n+1)} - V_I^{(n-1)}}{2\Delta t} + O\left(\Delta t^2\right)$$

$$\left(\frac{\mathrm{d}u_{s,k}}{\mathrm{d}t}\right)^{(n)} \approx \frac{u_{s,k}^{(n+1)} - u_{s,k}^{(n-1)}}{2\Delta t} + O\left(\Delta t^2\right)$$

$$\left(\frac{\mathrm{d}^2 u_{s,k}}{\mathrm{d}t^2}\right)^{(n)} \approx \frac{u_{s,k}^{(n+1)} - 2u_{s,k}^{(n)} + u_{s,k}^{(n-1)}}{(\Delta t)^2} + O\left(\Delta t^2\right)$$

Upon substituting these discretizations in Main text Eq. 3.10, we arrive at

$$\begin{aligned} &-\frac{2(-1)^k}{\pi k} \frac{V_I^{(n+1)} - V_I^{(n-1)}}{2\Delta t} + \frac{u_{s,k}^{(n+1)} - 2u_{s,k}^{(n)} + u_{s,k}^{(n-1)}}{(\Delta t)^2} + \\ &\nu_s \left(\frac{\pi k}{L_s}\right)^2 \frac{u_{s,k}^{(n+1)} - u_{s,k}^{(n-1)}}{2\Delta t} + \frac{2c_1}{\rho_s} \left(\frac{\pi k}{L_s}\right)^2 u_{s,k}^{(n)} + \frac{\pi k}{\rho_s L_s} \sigma_{\text{NL},k}^{(n)} + O\left(\Delta t^2\right) = 0 \end{aligned} \tag{9.10}$$

which upon algebraic manipulation leads to a second order temporally accurate solid displacement mode update

$$\begin{aligned} u_{s,k}^{(n+1)} = &\frac{1}{\zeta_{s,k}} \left[\frac{(-1)^k \Delta t \left(V_I^{(n+1)} - V_I^{(n-1)}\right)}{\pi k} + 2u_{s,k}^{(n)} - \left(2 - \zeta_{s,k}\right) u_{s,k}^{(n-1)} - \right. \\ &\left. (\Delta t)^2 \left(\frac{2c_1}{\rho_s} \left(\frac{\pi k}{L_s}\right)^2 u_{s,k}^{(n)} + \frac{\pi k}{\rho_s L_s} \sigma_{\text{NL},k}^{(n)} \right) \right] \end{aligned} \tag{9.11}$$

with

$$\zeta_{s,k} = 1 + \nu_s \frac{\Delta t}{2} \left(\frac{\pi k}{L_s}\right)^2 \tag{9.12}$$

Finally, we get a closed form for all the expressions by invoking the modal stress balance (Main text Eq. 3.11) at the $(n+1)^{\text{th}}$ time level below. Our choice of discretization at the $(n+1)^{\text{th}}$ step, rather than at the n^{th} step, ensures that the updates to the solid Eq. 9.11 and

fluid Eq. 9.6 modes are consistent with each other.

$$\underbrace{\left(\frac{\mu_f\left(V_{\text{wall}}-V_I\right)}{L_f}-\frac{2c_1U_I}{L_s}-\sigma_{\text{NL},0}-\frac{\mu_sV_I}{L_s}\right)}_{\text{I}}{}^{(n+1)}+\underbrace{\left(\sum_{k=1}^{\infty}\left[\frac{\mu_f\pi kv_{f,k}}{L_f}-(-1)^k\left\{\frac{2c_1\pi ku_{s,k}}{L_s}+\frac{\mu_s\pi k}{L_s}\frac{\mathrm{d}u_{s,k}}{\mathrm{d}t}+\sigma_{\text{NL},k}\right\}\right]\right)}_{\text{II}}{}^{(n+1)}=0 \tag{9.13}$$

In the above Eq. 9.13, we first describe the time discretization of the first term, denoted by the under-brace I. For this term, the nonlinear contribution σ_{NL} needs to be extrapolated forward in time to the $(n+1)^{\text{th}}$ step. To achieve this, we utilize the second-order accurate extrapolation EXT2 (Hairer *et al.* 1991) scheme whose formula is shown below.

$$\sigma_{\text{NL},0}^{(n+1)}\approx 2\sigma_{\text{NL},0}^{(n)}-\sigma_{\text{NL},0}^{(n-1)}+O\left(\Delta t^2\right) \tag{9.14}$$

This discretization is physically motivated by the fact that the nonlinear terms govern the evolution of *slow* non-linear elastic wave time scales $\sim O\left({L_s}^{-1}\left(c_3/\rho_s\right)^{0.5}\right)$ as opposed to the *fast* diffusive time scales $\sim O\left(L_s^2/\nu_s\right)$ in the system. Hence, we can extrapolate these stress waves forward in time and still capture the correct physics. Upon substituting the discretizations of Eqs. (9.4) and (9.14) in the term I discussed above, we arrive at

$$\text{I}\approx\frac{\mu_f\left(V_{\text{wall}}^{(n+1)}-V_I^{(n+1)}\right)}{L_f}-\frac{2c_1}{L_s}\left(U_I^{(n)}+\frac{\Delta t}{2}\left(V_I^{(n+1)}+V_I^{(n)}\right)\right)-(2\sigma_{\text{NL},0}^{(n)}-\sigma_{\text{NL},0}^{(n-1)})-\frac{\mu_sV_I^{(n+1)}}{L_s}+O\left(\Delta t^2\right) \tag{9.15}$$

Next, we discuss the time-discretization of the second term, denoted by the under-brace II in Eq. 9.13. The following formulae are used for discretizing the terms in this case

$$\left(\frac{\mathrm{d}u_{s,k}}{\mathrm{d}t}\right)^{(n+1)}\approx\frac{3u_{s,k}^{(n+1)}-4u_{s,k}^{(n)}+u_{s,k}^{(n-1)}}{2\Delta t}+O\left(\Delta t^2\right)$$

$$\sigma_{\text{NL},k}^{(n+1)}\approx 2\sigma_{\text{NL},k}^{(n)}-\sigma_{\text{NL},k}^{(n-1)}+O\left(\Delta t^2\right)$$

where the first discretization stems from the family of backward-difference formulae (BDF) (Hairer *et al.* 1991) and the second discretization is similar to Eq. 9.14. Upon

substituting these discretizations, the second term II now reads

$$\begin{aligned}\mathrm{II} \approx \sum_{k=1}^{\infty} \Bigg[& \frac{\mu_f \pi k v_{f,k}^{(n+1)}}{L_f} \\ & -(-1)^k \left\{ \frac{2c_1 \pi k u_{s,k}^{(n+1)}}{L_s} + \frac{\mu_s \pi k}{L_s} \left(\frac{3u_{s,k}^{(n+1)} - 4u_{s,k}^{(n)} + u_{s,k}^{(n-1)}}{2\Delta t} \right) + 2\sigma_{\mathrm{NL},k}^{(n)} - \sigma_{\mathrm{NL},k}^{(n-1)} \right\} \Bigg] \\ & + O\left(\Delta t^2\right)\end{aligned} \tag{9.16}$$

Now the terms at the $(n+1)^{\text{th}}$ step involving $v_{f,k}, u_{s,k}$ can be directly substituted with the previously derived modal update expressions (Eqs. (9.6) and (9.11)). Following Eq. 9.13 we set I + II = 0, using their discretized versions in Eqs. (9.15) and (9.16). After standard (but tedious) algebraic manipulations, we finally arrive at the update equation for the interface velocity $V_I^{(n+1)}$

$$V_I^{(n+1)} = \frac{E_I}{\frac{\mu_f}{L_f}\left(1 + 2\sum_{k=1}^{K-1} \frac{1}{\zeta_{f,k}}\right) + \frac{\mu_s}{L_s}\left(1 + \frac{3}{2}\sum_{k=1}^{K-1} \frac{1}{\zeta_{s,k}}\right) + \frac{c_1 \Delta t}{L_s}\left(1 + 2\sum_{k=1}^{K-1} \frac{1}{\zeta_{s,k}}\right)} \tag{9.17}$$

where

$$\begin{aligned} E_I = & \frac{\mu_f V_{\text{wall}}^{(n+1)}}{L_f} - \frac{c_1}{L_s}\left\{2U_I^{(n)} + (\Delta t) V_I^{(n)}\right\} - 2\sigma_{\mathrm{NL},0}^{(n)} + \sigma_{\mathrm{NL},0}^{(n-1)} \\ & + \sum_{k=1}^{K-1} \frac{\mu_f}{\zeta_{f,k} L_f}\left[\pi k(2 - \zeta_{f,k}) v_{f,k}^n + 2\left(V_I^{(n)} + (-1)^k \delta V_{\text{wall}}\right)\right] \\ & + \sum_{k=1}^{K-1} \frac{2c_1}{\zeta_{s,k} L_s}\left[V_I^{(n-1)} \Delta t + (-1)^k \pi k \left(\gamma_k u_{s,k}^{(n)} + (2 - \zeta_{s,k}) u_{s,k}^{(n-1)}\right)\right] \\ & + \sum_{k=1}^{K-1} \frac{\mu_s}{\zeta_{s,k} L_s \Delta t}\left[\frac{3}{2} V_I^{(n-1)} \Delta t + \right. \\ & \left. (-1)^k \pi k \left(\left\{\frac{3}{2}\gamma_k + 2\zeta_{s,k}\right\} u_{s,k}^{(n)} + \left\{\frac{3}{2}(2 - \zeta_{s,k}) - \frac{1}{2}\zeta_{s,k}\right\} u_{s,k}^{(n-1)}\right)\right] \\ & + \sum_{k=1}^{K-1} (-1)^k \left(\left\{\frac{\gamma_k + 2}{\zeta_{s,k}} + \frac{3}{2}\frac{\nu_s(\Delta t)}{\zeta_{s,k}}\left(\frac{\pi k}{L_s}\right)^2 - 2\right\} \sigma_{\mathrm{NL},k}^{(n)} + \sigma_{\mathrm{NL},k}^{(n-1)}\right) \end{aligned} \tag{9.18}$$

$$\gamma_k = \frac{2c_1}{\rho_s}\left(\frac{\pi k \Delta t}{L_s}\right)^2 - 2 \tag{9.19}$$

Overall, the above set of equations express the physical interface velocity, modal fluid velocities, modal solid displacements and physical interface displacement at a given time. Recovery of physical solid displacements and fluid velocities from their modal counterparts is achieved via Eq. 4.1. The system evolution can then be directly obtained by numerically iterating the above equations till the desired time. For convenience, the complete solution is

given below.

$$V_I^{(n+1)} = E_I \Big/ \left\{ \frac{\mu_f}{L_f}\left(1 + 2\sum_{k=1}^{K-1}\frac{1}{\zeta_{f,k}}\right) + \frac{\mu_s}{L_s}\left(1 + \frac{3}{2}\sum_{k=1}^{K-1}\frac{1}{\zeta_{s,k}}\right) + \frac{c_1\Delta t}{L_s}\left(1 + 2\sum_{k=1}^{K-1}\frac{1}{\zeta_{s,k}}\right)\right\}$$

$$u_{s,k}^{(n+1)} = \frac{1}{\zeta_{s,k}}\left[\frac{(-1)^k\Delta t\left(V_I^{(n+1)} - V_I^{(n-1)}\right)}{\pi k} + 2u_{s,k}^{(n)} - \left(2 - \zeta_{s,k}\right)u_{s,k}^{(n-1)} - (\Delta t)^2\left(\frac{2c_1}{\rho_s}\left(\frac{\pi k}{L_s}\right)^2 u_{s,k}^{(n)} + \frac{\pi k}{\rho_s L_s}\sigma_{\mathrm{NL},k}^{(n)}\right)\right]$$

$$v_{f,k}^{(n+1)} = \frac{E_{f,k}}{\zeta_{f,k}}; \qquad U_I^{(n+1)} = U_I^{(n)} + \frac{\Delta t}{2}\left(V_I^{(n+1)} + V_I^{(n)}\right);$$

with

$$\zeta_{s,k} = 1 + \nu_s\frac{\Delta t}{2}\left(\frac{\pi k}{L_s}\right)^2; \qquad \zeta_{f,k} = 1 + \nu_f\frac{\Delta t}{2}\left(\frac{\pi k}{L_f}\right)^2;$$

$$\delta V_{\mathrm{wall}} = V_{\mathrm{wall}}^{(n+1)} - V_{\mathrm{wall}}^{(n)}; \qquad \gamma_k = \frac{2c_1}{\rho_s}\left(\frac{\pi k\Delta t}{L_s}\right)^2 - 2;$$

$$E_{f,k} = \left(2 - \zeta_{f,k}\right)v_{f,k}^{(n)} - \frac{2\left\{V_I^{(n+1)} - V_I^{(n)} - (-1)^k\delta V_{\mathrm{wall}}\right\}}{\pi k}$$

$$\begin{aligned} E_I =& \frac{\mu_f V_{\mathrm{wall}}^{(n+1)}}{L_f} - \frac{c_1}{L_s}\left\{2U_I^{(n)} + (\Delta t)V_I^{(n)}\right\} - 2\sigma_{\mathrm{NL},0}^{(n)} + \sigma_{\mathrm{NL},0}^{(n-1)} \\ &+ \sum_{k=1}^{K-1}\frac{\mu_f}{\zeta_{f,k}L_f}\left[\pi k(2 - \zeta_{f,k})v_{f,k}^n + 2\left(V_I^{(n)} + (-1)^k\delta V_{\mathrm{wall}}\right)\right] \\ &+ \sum_{k=1}^{K-1}\frac{2c_1}{\zeta_{s,k}L_s}\left[V_I^{(n-1)}\Delta t + (-1)^k\pi k\left(\gamma_k u_{s,k}^{(n)} + (2 - \zeta_{s,k})u_{s,k}^{(n-1)}\right)\right] \\ &+ \sum_{k=1}^{K-1}\frac{\mu_s}{\zeta_{s,k}L_s\Delta t}\left[\frac{3}{2}V_I^{(n-1)}\Delta t + \right. \\ &\left.(-1)^k\pi k\left(\left\{\frac{3}{2}\gamma_k + 2\zeta_{s,k}\right\}u_{s,k}^{(n)} + \left\{\frac{3}{2}(2 - \zeta_{s,k}) - \frac{1}{2}\zeta_{s,k}\right\}u_{s,k}^{(n-1)}\right)\right] \\ &+ \sum_{k=1}^{K-1}(-1)^k\left(\left\{\frac{\gamma_k + 2}{\zeta_{s,k}} + \frac{3}{2}\frac{\nu_s(\Delta t)}{\zeta_{s,k}}\left(\frac{\pi k}{L_s}\right)^2 - 2\right\}\sigma_{\mathrm{NL},k}^{(n)} + \sigma_{\mathrm{NL},k}^{(n-1)}\right). \end{aligned}$$

10. Non-linear Kelvin–Voigt solid: Numerical least-squares fit procedure of the high-gain peak curves

In the case of the non-linear Kelvin–Voigt model, by spanning a phase-space numerically, we discover high-gain peaks similar to the linear Kelvin–Voigt case. These peaks seem to occur in a regular structure, but depart from the hyperbolic structures seen in the linear Kelvin–Voigt case. Then, to numerically characterize the curves on which these peaks reside, we use a numerical fit procedure which consists of the following steps. We begin by adopting a peak-detection algorithm to obtain all local maxima. We then cluster each maxima into its

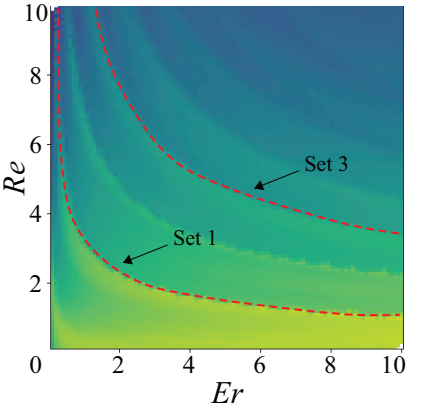

Figure 3: Clustering into sets, for further processing via the ANCOVA model (Keppel 1991)

own set, marked with a unique "set number" corresponding to the curve that the maxima lies on, see Fig. 3. This "set number" increases from 1 (bottom left) to n (top right) where n is the number of crests. We then fit the data using an ANCOVA model (Keppel 1991) with n sets, assuming the variation for a set i to be

$$Re = c_i Er^{\alpha}$$

where α is the exponent power and c_i is a scaling coefficient, both to be estimated. Here the subscript i in c_i indicates that it is allowed to vary between sets. We then report the α value, accurate up-to a significant digit.

11. Online sandbox for interactive simulations

The results presented in Sections 4 and 5.2 in the main text serve as a minimal platform for exploring flow–elastic structure interaction phenomena, thus building intuition into more complex problems. To aid this exploration, we open-source our computational code under a liberal license. Further, to enable a seamless research/educational experience and to disencumber scientists/students from the process of installing essential computational software stack, we provide an interactive sandbox built atop our code. This sandbox is free, open-source, hosted online and is accessible from any modern web browser running on personal devices from mobile phones to laptops. Our sandbox can be found here and the numerical code powering it is available here. We present snapshots of this sandbox in Fig. 4. Users can utilize simple sliders to change geometrical and dynamical parameters on the left, which are then used to run computations asynchronously before presenting results and velocity plots on the right.

REFERENCES

Ayoub, Muhammad & Abdullah, Ahmad Zuhairi 2012 Critical review on the current scenario and significance of crude glycerol resulting from biodiesel industry towards more sustainable renewable energy industry. *Renewable and Sustainable Energy Reviews* **16** (5), 2671–2686.

Bhosale, Yashraj, Parthasarathy, Tejaswin & Gazzola, Mattia 2021 A remeshed vortex method for mixed rigid/soft body fluid–structure interaction. *Journal of Computational Physics* p. 110577.

Cheng, Nian-Sheng 2008 Formula for the viscosity of a glycerol- water mixture. *Industrial & engineering chemistry research* **47** (9), 3285–3288.

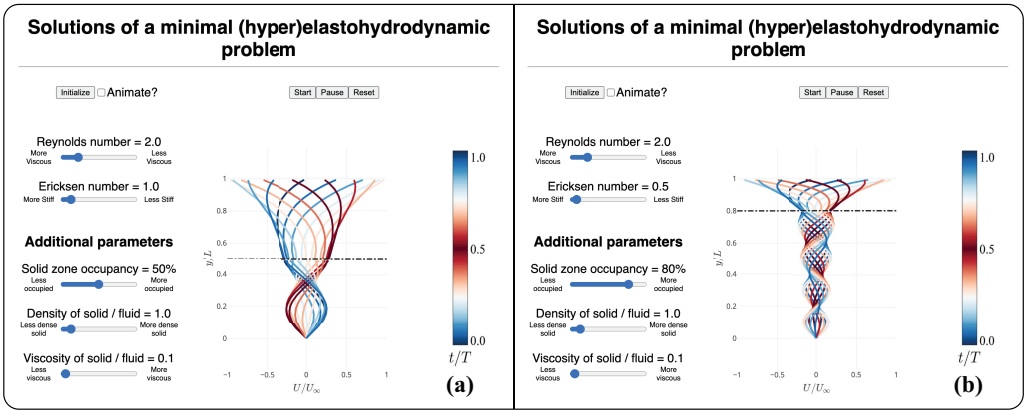

Figure 4: Online sandbox. Using sliders to control the geometrical and dynamical parameters, users can investigate the response of the system for a wide range of parameters, shown for two representative cases. Here the settings of (*a*) corresponds to the $Re = 2$, $Er = 1$ case, whose profiles were discussed earlier in Fig. 3. Changing the solid properties (elasticity via Er, occupancy via L_f/L_s and density via ρ) leads to the profiles shown in (*b*). In both cases, the interface is marked with a solid, black line for visual clarity.

Desprat, N, Guiroy, A & Asnacios, A 2006 Microplates-based rheometer for a single living cell. *Review of scientific instruments* **77** (5), 055111.

Duncombe, Todd A, Tentori, Augusto M & Herr, Amy E 2015 Microfluidics: reframing biological enquiry. *Nature Reviews Molecular Cell Biology* **16** (9), 554–567.

Guimarães, Carlos F, Gasperini, Luca, Marques, Alexandra P & Reis, Rui L 2020 The stiffness of living tissues and its implications for tissue engineering. *Nature Reviews Materials* **5** (5), 351–370.

Hairer, Ernst, Nørsett, Syvert P & Wanner, Gerhard 1991 *Solving ordinary differential equations I, Nonstiff problems*. Springer-Vlg.

Keppel, Geoffrey 1991 *Design and analysis: A researcher's handbook*. Prentice-Hall, Inc.

Landau, LD & Lifshitz, EM 1987 Theoretical physics, vol. 6, fluid mechanics.

Leclaire, S, Pellerin, N, Reggio, M & Trépanier, JY 2014 Unsteady immiscible multiphase flow validation of a multiple-relaxation-time lattice boltzmann method. *Journal of Physics A: Mathematical and Theoretical* **47** (10), 105501.

Shankaran, Harish & Neelamegham, Sriram 2001 Effect of secondary flow on biological experiments in the cone-plate viscometer: Methods for estimating collision frequency, wall shear stress and inter-particle interactions in non-linear flow. *Biorheology* **38** (4), 275–304.

Sim, Woo-Gun 2006 Stratified steady and unsteady two-phase flows between two parallel plates. *Journal of mechanical science and technology* **20** (1), 125.

Sugiyama, Kazuyasu, Ii, Satoshi, Takeuchi, Shintaro, Takagi, Shu & Matsumoto, Yoichiro 2011 A full eulerian finite difference approach for solving fluid–structure coupling problems. *Journal of Computational Physics* **230** (3), 596–627.

Volk, Andreas & Kähler, Christian J 2018 Density model for aqueous glycerol solutions. *Experiments in Fluids* **59** (5), 1–4.

Wu, Pei-Hsun, Aroush, Dikla Raz-Ben, Asnacios, Atef, Chen, Wei-Chiang, Dokukin, Maxim E, Doss, Bryant L, Durand-Smet, Pauline, Ekpenyong, Andrew, Guck, Jochen, Guz, Nataliia V & others 2018 A comparison of methods to assess cell mechanical properties. *Nature methods* **15**, 491–498.